Quantifying chiral exchange interaction for Néel-type skyrmions via Lorentz transmission electron microscopy

Wanjun Jiang[1,2,*,†], Sheng Zhang[2,3]*, Xiao Wang[2,4,*], Charudatta Phatak[2,†],
Qiang Wang[2,5], Wei Zhang[2,6], Matthias Benjamin Jungfleisch[2,7],
John E. Pearson[2], Yizhou Liu[8], Jiadong Zang[9], Xuemei Cheng[4],
Amanda Petford-Long[2], Axel Hoffmann[2] and Suzanne G. E. te Velthuis[2,†]

[1]State Key Laboratory of Low-Dimensional Quantum Physics and Department of Physics, Tsinghua University, Beijing 100084, China

[2]Materials Science Division, Argonne National Laboratory, Lemont, Illinois, USA, 60439

[3]Advanced Science Research Center, The City University of New York, 85 Saint Nicholas Terrace, New York, NY, USA, 10031

[4]Department of Physics, Bryn Mawr College, Bryn Mawr, PA, USA, 19010

[5]Department of Physics and Astronomy, West Virginia University, Morgantown, WV, USA, 26506

[6]Department of Physics, Oakland University, Rochester, MI, USA, 48309

[7]Department of Physics and Astronomy, University of Delaware, Newark, DE, USA, 19716

[8]Beijing National Laboratory for Condensed Matter Physics and Institute of Physics, Chinese Academy of Sciences, Beijing 100190, China

[9]Department of Physics, University of New Hampshire, Durham, NH, USA, 032824

*These authors contributed equally.

†To whom correspondence should be addressed.

E-mail: jiang_lab@tsinghua.edu.cn, cd@anl.gov, tevelthuis@anl.gov

Abstract

Magnetic skyrmions are topological spin textures that have been observed in bulk magnets and magnetic multilayers. For bulk magnetic materials, their non-collinear spin profiles have often been studied by using Lorentz transmission electron microscopy (TEM). In this report, we experimentally utilized Lorentz TEM imaging to study an inversion asymmetric [Pt(1.5nm)/Co(1nm)/W(1nm)]$_8$ heterostructure that exhibits Néel-type skyrmions at zero field. By tracking the evolution of skyrmion diameters as a function of magnetic fields, we determined the strength of the interfacial Dzyaloshinskii-Moriya interaction (DMI). Our results suggest that in-situ Lorentz TEM imaging combined with simulations can provide valuable quantitative information about the interfacial DMI strengths, which can be helpful for optimizing skyrmion materials. Furthermore, we show that in theory Lorentz TEM can identify the spin chirality of Néel-type skyrmions, although an experimental verification is challenging due to the relatively low signal-to-noise ratio.

Introduction

Magnetic skyrmions were first identified in the non-centro-symmetric B20 bulk magnets, such as MnSi, FeGe, FeCoSi compounds, where the existence of an anti-symmetric Dzyaloshinskii-Moriya interaction (DMI) favors (vortex-like) Bloch-type skyrmions.[1-9] In contrast to the symmetry breaking of the crystal structure in the typical B20 compounds, one can also synthesize magnetic heterostructures that artificially break the inversion symmetry via the presence of interfaces.[10-16] In multilayers, which typically consist of heavy metal/ultra-thin ferromagnet/(insulator or different metal), the interfacial symmetry breaking also introduces a DMI component that generates noncollinear spin textures.[10-14,17-24] This interfacial DMI is mediated by the adjacent heavy metal layer and can be expressed as $-\boldsymbol{D}_k \cdot (\boldsymbol{S}_i \times \boldsymbol{S}_j)$, where $\boldsymbol{S}_i$ and $\boldsymbol{S}_j$ are neighboring (canted) atomic spin vectors, $\boldsymbol{D}_k$ is the DMI vector lying in the interfacial plane that energetically favors Néel-type (*i.e.*, hedgehog-like) skyrmions,[10,11,24-29] as compared to the Bloch-type (*i.e.*, vortex-like) spin textures in most bulk materials. Note that the sign of the DMI vector $\boldsymbol{D}_k$ determines the handedness (spin chirality) of Néel-type skyrmion to be left or right. While the real-space spin configurations are quite different for the Bloch- or Néel-type skyrmions, their topological properties remain equivalent. Namely, the skyrmion number $Q = {}^{1}/_{4\pi} \int \boldsymbol{m} \cdot \left(\partial_x \boldsymbol{m} \times \partial_y \boldsymbol{m}\right) dxdy$, which is defined by wrapping the spin unit vector ($\boldsymbol{m}$) around a unit sphere, is identical.[6,8] Note that, Néel-type skyrmions were also observed in bulk Lacunar spinel GaV_4S_8 with a C_{nv} symmetry.[30]

Beyond exhibiting room-temperature nanoscale skyrmions, in magnetic multilayers, the spin Hall effects of the heavy metal layer give rise to current-induced spin-orbit torques[31-36] that result in efficient electrical creation and/or manipulation of spin textures.[25,29,37-40] In particular, the insertion of a thin ferromagnetic layer in between two different heavy metal layers could provide complementary spin orbit torques, for efficient manipulation and additive interfacial DMIs, as well as for size miniaturization, given a proper choice of various materials. Magnetic multilayers are thus more technologically promising for enabling functional skyrmionic logic/memory,[13,14,24,36,37] and tremendous effort has recently been devoted towards this goal.[28,29,41,42] For example, multilayers based on Pt/Co/Ta, Pt/CoFeB/MgO, W/CoFeB/MgO, and Pt/Co/Ir trilayers have been synthesized in which electrical generation, manipulation, and detection of magnetic skyrmions were demonstrated.[28,29,42-44] Here, we demonstrate the stabilization of zero-field nanoscale skyrmions in another system – Pt/Co/W multilayers. Our work is motivated by the fact that Pt/Co/W trilayers are expected to be energetically advantageous for boosting the motion of magnetic skyrmions.[45] This is because the spin Hall angles (θ_{sh}) at the two interfaces of each Co layer have opposite sign, which thus provide complementary spin Hall torques.[28,29,34] Namely, the spin Hall angle of Pt is $\theta_{sh} \approx +10\%$ and W is $\theta_{sh} \approx -35\%$. Thus spin-orbit torques from the two layers are expected to act constructively due to the opposite orientation with respect to the ferromagnet at their respective interfaces.[45,46]

Lorentz TEM has been extensively utilized for studying the non-collinear spin textures.[3,5,8,9,47-57] Here we first discuss theoretical expressions for, and calculate, the magnetic contrast in the Lorentz TEM images for Néel-type skyrmions ($Q = \pm 1$). This will subsequently be used to demonstrate the experimental detection of Néel-type skyrmions with Lorentz TEM and investigate the dependence of skyrmion size as a function of magnetic field in a Pt/Co/W multilayer. Analyzing this dependence allows us then to quantify the interfacial DMI.

Modeling Lorentz TEM imaging

The calculation of magnetic contrast in Lorentz TEM images is based on a simplified relation describing the phase shift of the electron wave upon passing through a magnetic sample, which can be detected by defocusing the objective lens of the microscope.[55,58,59] Namely, magnetic contrast in the Lorentz TEM images can be experimentally observed when the focus length $\Delta f \neq 0$, *i.e.*, out-of-focus condition and only in the regions that have a non-zero gradient of the phase shift ($\nabla\varphi \neq 0$).[60,61] For example, a nonzero phase shift $\tilde{\varphi}_m(\boldsymbol{k})$ can be obtained for Bloch-type skyrmion in the Lorentz TEM. Note that the same relationship can also be used to correlate the observed magnetic contrast with the gradient of phase shifts.[58]

The phase shift for Néel-type (hedgehog) skyrmions and the corresponding image intensity in Lorentz TEM images can also be calculated as[60,61]:

$$\tilde{\varphi}_m(\boldsymbol{k}) = -X\frac{2\pi^2\mu_0 M_s}{\phi_0}\frac{D_2 J_1(k_\perp D_2)}{k_\perp^3}\left(k_x k_y - k_y k_x\right) \equiv 0. \tag{1}$$

Here $X = \pm 1$ defines the chirality of the skyrmion, μ_0 is the vacuum permeability, M_s is the saturation magnetization, $\phi_0 = {}^{h}\!/_{2e} = 2.07 \times 10^3\ \mathrm{T\ nm}^2$ is the flux quanta, D_2 is the width of the spin transition regime/domain wall, J_1 is the first order Bessel function and $k_\perp = \sqrt{k_x^2 + k_y^2}$ is the Fourier wave vector. This shows that the contribution to the phase shift from the in-plane components of the Néel-type skyrmion is zero, and thus the out-of-focus Lorentz TEM images for a film that is normal to the incident electron beam do not contain any magnetic contrast.

Change of Phase Shift by Tilting the Sample

Although *Eq.*1 implies that Lorentz TEM is insensitive to Néel-type skyrmions, phase shifts of Néel-type skyrmions/domain walls have in fact been observed when the sample is tilted away from the normal incidence.[44,62,63] We will subsequently discuss the effect of tilting the sample in more detail. By tilting the sample about the x-axis by an arbitrary angle Φ, the new magnetization vectors in all three regions defining the Néel skyrmion (see Fig. 1) can be written as in the region outside of the skyrmion R_1: $M_1 = M_s(0, -\sin\Phi, \cos\Phi)$, inside the skyrmions core R_3: $M_3 = M_s(0, \sin\Phi, -\cos\Phi)$, and along the domain wall in between these two regions R_2: $M_2 = M_s(\cos\theta, \cos\Phi\sin\theta, -\sin\Phi\cos\theta)$. Of these only the x and y components are of importance. The contribution from region R_2 can be calculated as follows:

$$\tilde{\varphi}_m(\boldsymbol{k})_{R_2} = C\big((k_x)k_y - (k_y cos\Phi)k_x\big) = Ck_xk_y(1 - cos\Phi), \qquad (2)$$

where C contains all the prefactors and other terms depending on k_x and k_y. This shows that the phase shift from region R_2 is non-zero upon tilting the sample and increases slowly as a function of Φ due to the dependence on $(1 - cos\Phi)$.

Lorentz TEM Image Simulations

We will now explore the effect on the magnetic contrast with and without tilting the sample with respect to the incident electron beam. These simulations were carried out for an ultra-thin Co thin film with thickness of 1 nm and magnetic field B_0= 1.7 T. The microscope parameters used were E = 200 kV, and a defocus value of 100 µm. The size of these bubble-shaped spin textures is 100 nm in diameter and domain wall width (D_2) is fixed as 20 nm (width of region R_2).

Lorentz TEM images were simulated for three different tilting angles $\Phi = -60^{\circ}$, $\Phi = -0^{\circ}$, and $\Phi = +60^{\circ}$, shown in Fig. 1. The tilting axis is along the horizontal direction () as indicated by the schematic and red arrow. We consider two different types of Néel-type skyrmions with opposite spin chirality (left-handed and right-handed) as shown in Figs. 1A and 1B. Note that the handedness of chiral spin structures is determined by the sign of interfacial DMI. As expected at zero tilting angle (normal incidence), no visible magnetic contrast is observed. For the tilted configurations, the introduced contrast is due to the in-plane projection of the perpendicular magnetization from regimes R_1 and R_3, respectively. As a result, the switching of the black and white contrasts for opposite tilting angles is observed. These simulations show that it is possible to detect Néel skyrmions with Lorentz TEM if the sample is tilted.[62,63]

Chirality of Néel-type skyrmions

Chirality is one of the distinguishing parameters for identifying Néel-type skyrmions, and can be either left handed or right handed. The physical origin of the chirality depends on the spin-orbit coupling at the interface.[22] While the chirality can be inferred based on the sign of the interfacial DMI and on the direction of skyrmion (or chiral domain wall) motion, it is also useful to image it directly. As discussed earlier, Néel-type skyrmions are visible using Lorentz TEM, *i.e.*, giving rise to contrast in the image, only when the sample is tilted away from normal incidence. The primary effect of this tilting is due to the introduction of an in-plane component of magnetization from the out-of-plane magnetization regions. Additionally, a slight asymmetry in the image contrast is also introduced from regime R_2, which has an in-plane magnetization configuration. The introduced asymmetry in the image contrast and its relation to chirality of Néel-type skyrmions can be related to the orientation of the magnetization in the regime R_2. As the sample is tilted, there is a difference in the remanent in-plane components of the magnetization in regime R_2 which is dependent upon chirality. For example, in case of a Néel-type skyrmion where the magnetization in regime R_2 points radially inwards, and for a sample tilt as shown in Fig. 1 (top row), the in-plane magnetization components in the top half of regime R_2 will not be the same as the bottom half. This will be the reverse case for Néel-type skyrmion with magnetization pointing radially outwards. In the ultimate limiting case of tilting by 90°, one can think of imaging two 180° Néel domain walls which are either convergent or divergent, *i.e.*, depending on the chirality of the Néel-type skyrmion.

This suggests there is a magnetic contrast difference for Néel-type skyrmions with opposite chirality. However, this difference will be very small as compared to the contrast originating from regimes R_1 and R_3. One method to potentially view this contrast difference is to take the average of the two out-of-focus images at opposite tilt angles so that the contribution from regimes R_1 and R_3 is removed. This method is verified with a simulation using a tilt angle $\Phi = \pm 60^{\circ}$, in which a contrast difference between the averaged images for the two opposite chiralities can be observed, as shown in the Fig. 1, However, the magnetic contrast due to the chirality difference is very weak (~18%). Such a small contrast difference is challenging to measure experimentally since it requires a precise alignment of the out-of-focus images (given the width of the magnetic domain wall in the ultrathin film, which is around 10 nm, as determined by the exchange stiffness and uniaxial anisotropy). Note that the diffraction contrast arising from the microstructure in thin films also contributes to additional noise in the images. In the following, a Lorentz TEM will be used to experimentally probe the magnetic contrast of Néel-type skyrmions in a thin film.

Material system

The nominal composition and thickness of the multilayer system studied are: Ta(2 nm)/[Pt(1.5 nm)/Co(1 nm)/W(1 nm)]$_8$/Pt(1.5 nm), as schematically shown in Fig. 2A. Our multilayer was grown using dc magnetron sputtering under a 3-mTorr Ar pressure onto a semi-insulating Si substrate covered with 300-nm thermally oxidized SiO_2. The Lorentz TEM specimen was grown onto 2×2 mm^2 TEM grids with a 50-nm thick silicon nitride (SiN_x) membrane. The bottom 2-nm Ta was grown as a seed layer. The base pressure of the sputtering chamber was typically < 10^{-8} Torr. The sputtering rates for Ta, Pt, Co and W were 0.4 $\mathrm{\AA}$/s, 0.5 $\mathrm{\AA}$/s, 0.2 $\mathrm{\AA}$/s and 0.2 $\mathrm{\AA}$/s, respectively. A Quantum Design superconducting quantum interference device (SQUID) magnetometer was used to measure the hysteresis loops with in-plane and out-of-plane applied magnetic fields. An X-ray diffractometer of model PANalytical X'Pert MRD with Cu K_α emission (1.5405 $\mathrm{\AA}$) was used for the X-ray reflectivity measurement. The zero-field Lorentz TEM experiments were performed in a JEOL 2100F instrument with a spherical aberration corrector. The corresponding out-of-focus Fresnel imaging mode was used with a defocus value of 6.4 mm. A FEI Tecnai F20ST TEM/STEM system was subsequently used to acquire field dependent magnetic images in the Lorentz mode by adjusting the objective lens current with the tiling angle fixed at 30° and a defocus value of 9.72 mm. All experiments were carried out at room temperature.

In order to analyze the interface characteristics of our multilayer sample, we have carried out X-ray reflectivity measurements. The superlattice peaks are clearly visible to the third order, indicating a high degree of crystallographic perfection along the growth direction, as shown in the right of Fig. 2B. To determine the depth-dependent scattering-length density (SLD) profile, we used a Parratt formalism to fit the X-ray reflectivity data.[64,65] The data analysis yields the roughness (Δt), and the thickness (t) of each individual layer, which is consistent with the expected nominal thicknesses (t_n), as summarized in Table 1. We have also carried out magnetometry measurements of magnetic hysteresis (*M*-*H*) loops, measured perpendicular to the plane ($H_{\perp}$), and shown in the inset to Fig. 2B. These measurements demonstrate that the sample has a perpendicular magnetic anisotropy, with a saturation magnetization $M_s = 1.2 \times 10^6$ A/m, and a perpendicular anisotropy field H_k= 0.35 T.

Imaging experiments

Lorentz TEM imaging experiments were performed in a field-free environment using a JEOL 2100F instrument with a spherical aberration corrector, which enables imaging of magnetic structures at a spatial resolution as high as a few nanometers depending on the material and defocus. Before conducting Lorentz TEM imaging experiment, the sample was demagnetized by applying an in-plane magnetic field of 1 Tesla. This process is essential for ensuring the existence of skyrmions at zero field. With the sample untilted, no observable magnetic contrast is seen in the under-focus images shown in Fig. 3B. The only contrast results from the presence of grains in the film. When the sample is tilted by $\Phi = -30^{\circ}$ away from the plane normal, randomly distributed bubble-like and stripe-like spin textures were clearly revealed as shown in Fig. 3A. In each case the upper left side of each feature appears black and the lower right side appears white. This contrast reverses upon inverting the tilting angle to $\Phi = +30^{\circ}$, as shown in Fig. 3C, suggesting that the magnetic structures are Néel-type skyrmions, consistent with the simulations shown in Fig. 1. The size of skyrmion is defined as the peak-to-dip distance of the intensity profiles along the diagonal direction, as shown in Fig. 3D. The size of these skyrmions varies spatially, which can likely be linked to the spatial variation of the local magnetic properties, including anisotropy, magnetization and DMI due to the natural presence of impurities, defects, grain orientations, and film roughness. Note that the size of the skyrmions from the out-of-focus images is further calibrated by using a lithographically-patterned microstructure using the same microscope parameters.

In-situ magnetizing experiments were also performed on this $[Pt/Co/W]_8$ multilayer sample using Lorentz mode in a FEI Tecnai F20ST TEM/STEM. The strength of the vertical applied field was controlled by adjusting the objective lens current. The sample was tilted to 30°. As the external perpendicular magnetic field, H_z, is gradually increased starting from zero, both the size and the density of skyrmions decreases monotonically, as shown in the Figs. 4A – D. A minimum skyrmion size, $d_0 = 220 \ \pm 10$ nm, is seen, as shown in Fig. 4E. Further increasing the magnetic field results in annihilation of the skyrmions in the (total) magnetic field range between 20 mT and 25 mT, rather than a continuous shrinking of size. After saturation, Lorentz TEM imaging along the hysteresis loop by decreasing magnetic field is also performed, which reveals labyrinthine stripe domains with widths of which are comparable with the diameter of skyrmions.

Discussion

The formation of Néel-type skyrmion in the multilayer is favored by the interfacial DMI. By studying the evolution of the skyrmion size as a function of magnetic field, one can determine the value/ of the interfacial DMI. This can be done by applying the scaling laws for an effective-medium model. In this model, the magnetic multilayers were considered as an effective thin film due to the coherency of the magnetization in each layer,[29,40] and the reduced (volume) self-energy $\widehat{U}$ (that is normalized by $2\pi^2 M_s^2 h^3$) of each individual, isolated, skyrmion can be expressed as follows:

$$\widehat{U} = [N_B + H_a - 1]\left(\frac{d}{h}\right)^2 + \frac{4d}{M_s^2 h^2}\delta_{dw}, \tag{3}$$

where M_S is the saturation magnetization, d is the diameter of the skyrmion, h is the effective thickness, $N_B = 1 + \frac{4}{3\pi}\cdot\frac{d}{h}\{1 - k^{-3}[(1-k^2)K + (2k^2-1)E]\}$ with E and K are being complex elliptical integrals of $k = \frac{d}{h}\left[\left(\frac{d}{h}\right)^2 + 1\right]^{-1/2}$. H_a is the dimensionless external magnetic field $H_a = {}^{H_z}/_{M_s}$, and the domain wall surface energy density δ_{dw} is further given by:[20,29,40]

$$\delta_{dw} = 4\sqrt{AK_{eff}} - \pi|D_k|, \tag{4}$$

where A is the spin-wave exchange stiffness, and K_{eff} is the effective perpendicular anisotropy energy density. Inserting experimentally-determined parameters into the above equations, the reduced energy $\widehat{U}$ as a function of skyrmion diameter d can be calculated for a given value of D_k. For our [Pt/Co/W]$_8$ multilayers the $A = 10\ \mathrm{pJ/m}$ was used,[28] perpendicular anisotropy field: $H_k = 0.3$ T, saturation magnetization $M_s = 1.2 \times 10^6\ \mathrm{A/m}$, which results in an effective anisotropy energy density: $K_{eff} = 6.62 \times 10^5\ \mathrm{J/m^3}$.

The DMI strength can be found, by determining the value of D_k for which the experimentally determined skyrmion sizes correspond to the local minimum of $\widehat{U}$. In Fig. 5, the reduced energy $\widehat{U}$ of isolated magnetic skyrmions as a function of diameter d are plotted for different D_k at several applied fields (7.6 mT, 12.1 mT, 21 mT and 25 mT). The three-black dashed/dotted curves in each graph are the theoretically calculated energy-diameter dependences for D_k = 1.3 mJ/m^2, 1.5 mJ/m^2, and 1.7 mJ/m^2. A stable skyrmion state is energetically favored at the energy minima. The experimentally observed skyrmion sizes, shown as vertical dashed lines, are close to the local energy minima at all fields when D_k = 1.5 mJ/m^2, indicating this is the DMI strength of the system. When D_k = 1.3 mJ/m^2 or 1.7 mJ/m^2 the skyrmion sizes already do not coincide with the minima as well or only for a limited range of fields. Subsequently, the error in the determined value of D_k is estimated to be at most 0.2 mJ/m^2. Note that the minima in the calculations are relatively shallow, which therefore results in a broad size distribution of the skyrmions in the presence of even moderate pinning due to materials imperfections. Furthermore, this may explain why the size evolution with field does not follow the ideal behavior expected from the calculated positions of the minima of the energy, but rather might be determined by a critical energy gradient in order to overcome local pinning. As shown in Fig. 5, the skyrmion diameter decreases following an increase of the external magnetic fields. At a magnetic field of 7.6 mT, the skyrmion diameter lies in a range of 200 nm to 700 nm. Experimentally, we have also observed a minimum diameter of value $d_0 = 220 \ \pm 10$ nm below which the skyrmion state vanishes and following an increase in applied magnetic fields, the system evolves into a pure ferromagnetic state. Our calculation also captures qualitatively this feature, *viz*., the less pronounced and subsequent disappearance of the local energy minimum in the calculation as the field increases suggests that the skyrmion phase become less energetically stable.

To validate the effective-medium model, we further performed micromagnetic simulations using Mumax3 software.[66] A thin film with 1 μm × 1 μm lateral size and 1 nm thickness was simulated. The material specific parameters for Pt/Co/W multilayer are: exchange constant A = 10 pJ/m, perpendicular magnetic anisotropy constant K_u = 1.24×10^6 J/m^3 and saturation magnetization M_s = 1.2×10^6 A/m. Size evolution of skyrmions for three different positive DMI values, D_k = 1.4 mJ/m^2, D_k = 1.5 mJ/m^2 and D_k = 1.6 mJ/m^2 were studied. The simulated skyrmion sizes as a function of perpendicular magnetic fields are shown in Fig. 6, which demonstrate clearly that the tendency of experimental data shown in Fig. 4E can be qualitatively reproduced. Based on the first principle calculation results and other experimental results in similar multilayers, a left-handed Néel-type skyrmion is more energetically favorable in the present system.[22,28] This is also indirectly confirmed by our micromagnetic simulation. Experiments at large tilting angles ($\Phi = \pm 60^{\circ}$) are also conducted, a precise imaging alignment is challenging due to the relatively low signal-to-noise ratio in Lorentz TEM imaging. Thus, a direct visualization of spin chirality is not available from the present experimental study. Note that the influence of interlayer dipolar interactions and material defects was not considered. Furthermore, the simulated results shown in Fig. 6 reveals a minimum value around 74 nm that is also consistent with experimental observations. Our simulations suggest that, around the minimum diameter, the skyrmion with a large inner core was transformed into a compact skyrmion (Fig. 6 insets) due to the increase of the Zeeman energy.[67] Further increasing the applied fields, however, results in its collapse due to the fact that DMI energy is insufficient to stabilize compact skyrmions in the presence of the enhanced Zeeman energy. Our micromagnetic simulation thus confirms that the effect-medium approach captures the physics of skyrmions in multilayers.

Conclusion

In summary, we have derived expressions for the phase shift in the Lorentz TEM imaging for Néel-type skyrmions. Our work illustrates that it is in principle possible to determine the chirality of the Néel-type skyrmions, but experimentally it will be challenging to obtain sufficient signal-to-noise ratio. We subsequently carried out Lorentz TEM experiments in an inversion-asymmetric $[\mathrm{Pt/Co/W}]_8$ multilayer, where the stabilization of room-temperature Néel-type skyrmions in the absence of a magnetic field is achieved. Based on an effective model, we estimated the strength of the interfacial DMI to be $D_k = 1.5 \pm 0.2\ \mathrm{mJ/m^2}$ from measurements of skyrmion size as a function of applied magnetic fields. Similar behavior is determined from micromagnetic simulation studies. One advantage of stabilizing skyrmions in $[\mathrm{Pt/Co/W}]_8$ multilayers is the potential for simultaneously exploiting additive interfacial DMIs and complimentary SOTs.[28,29,68,69]

Acknowledgements

Work performed at Tsinghua, including data analysis and manuscript preparation, was supported by National Key R&D Program of China under contract number 2017YFA0206200, 2016YFA0302300, NSF of China under contract number (11774194, 51831005, 11861131008) and the Beijing Advanced Innovation Center for Future Chip (ICFC). Work carried out at the Argonne National Laboratory, including all experimental aspects, data analysis, and manuscript preparation, was supported by the U.S. Department of Energy, Office of Science, Materials Science and Engineering Division. Work at Bryn Mawr College was supported by NSF CAREER award (No. 1053854) and NSF DMR (No.1708790). Micromagnetic simulation carried out by University of New Hampshire was supported by the U.S. Department of Energy (DOE), Office of Science, Basic Energy Sciences (BES) under Award No. DE-SC0016424.

References

1 Rossler, U. K., Bogdanov, A. N. & Pfleiderer, C. *Nature* **442**, 797-801 (2006).

2 Mühlbauer, S., Binz, B., Jonietz, F., Pfleiderer, C., Rosch, A., Neubauer, A., Georgii, R. & Böni, P. *Science* **323**, 915-919 (2009).

3 Yu, X. Z., Onose, Y., Kanazawa, N., Park, J. H., Han, J. H., Matsui, Y., Nagaosa, N. & Tokura, Y. *Nature* **465**, 901-904 (2010).

4 Jonietz, F., Mühlbauer, S., Pfleiderer, C., Neubauer, A., Münzer, W., Bauer, A., Adams, T., Georgii, R., Böni, P., Duine, R. A., Everschor, K., Garst, M. & Rosch, A. *Science* **330**, 1648-1651 (2010).

5 Yu, X. Z., Kanazawa, N., Onose, Y., Kimoto, K., Zhang, W. Z., Ishiwata, S., Matsui, Y. & Tokura, Y. *Nature Materials* **10**, 106-109 (2011).

6 Braun, H. B. *Advances in Physics* **61**, 1-116 (2012).

7 Schulz, T., Ritz, R., Bauer, A., Halder, M., Wagner, M., Franz, C., Pfleiderer, C., Everschor, K., Garst, M. & Rosch, A. *Nature Physics* **8**, 301-304 (2012).

8 Nagaosa, N. & Tokura, Y. *Nature Nanotechnology* **8**, 899-911 (2013).

9 Du, H., Che, R., Kong, L., Zhao, X., Jin, C., Wang, C., Yang, J., Ning, W., Li, R., Jin, C., Chen, X., Zang, J., Zhang, Y. & Tian, M. *Nature Communications* **6**, 8504 (2015).

10 Fert, A., Cros, V. & Sampaio, J. *Nature Nanotechnology* **8**, 152-156 (2013).

11 Sampaio, J., Cros, V., Rohart, S., Thiaville, A. & Fert, A. *Nature Nanotechnology* **8**, 839-844 (2013).

12 R. Tomasello, E. Martinez, R. Zivieri, L. Torres, M. Carpentieri & Finocchio, G. *Scientific Reports* **4**, 6784 (2014).

13 Wiesendanger, R. *Nat Rev Mater* **1**, 16044 (2016).

14 Fert, A., Reyren, N. & Cros, V. *Nat Rev Mater* **2**, 17031 (2017).

15 Chen, G., Mascaraque, A., N'Diaye, A. T. & Schmid, A. K. *Appl Phys Lett* **106**, 242404 (2015).

16 Dupe, B., Bihlmayer, G., Bottcher, M., Blügel, S. & Heinze, S. *Nature Communications* **7**, 11779 (2016).

17 Bogdanov, A. N. & Rößler, U. K. *Physical Review Letters* **87**, 037203 (2001).

18 Bode, M., Heide, M., von Bergmann, K., Ferriani, P., Heinze, S., Bihlmayer, G., Kubetzka, A., Pietzsch, O., Blügel, S. & Wiesendanger, R. *Nature* **447**, 190-193 (2007).

19 Heinze, S., von Bergmann, K., Menzel, M., Brede, J., Kubetzka, A., Wiesendanger, R., Bihlmayer, G. & Blügel, S. *Nature Physics* **7**, 713-718 (2011).

20 Thiaville, A., Rohart, S., Jue, E., Cros, V. & Fert, A. *Europhysics Letters* **100**, 57002 (2012).

21 Chen, G., Zhu, J., Quesada, A., Li, J., N'Diaye, A. T., Huo, Y., Ma, T. P., Chen, Y., Kwon, H. Y., Won, C., Qiu, Z. Q., Schmid, A. K. & Wu, Y. Z. *Physical Review Letters* **110**, 177204 (2013).

22 Yang, H., Thiaville, A., Rohart, S., Fert, A. & Chshiev, M. *Physical Review Letters* **115**, 267210 (2015).

23 Soumyanarayanan, A., Reyren, N., Fert, A. & Panagopoulos, C. *Nature* **539**, 509-517 (2016).

24 Jiang, W., Chen, G., Liu, K., Zang, J., te Velthuis, S. G. E. & Hoffmann, A. *Physics Reports-Review Section of Physics Letters* **704**, 1-49 (2017).

25 Jiang, W., Upadhyaya, P., Zhang, W., Yu, G., Jungfleisch, M. B., Fradin, F. Y., Pearson, J. E., Tserkovnyak, Y., Wang, K. L., Heinonen, O., te Velthuis, S. G. E. & Hoffmann, A. *Science* **349**, 283-286 (2015).

26 Chen, G., Mascaraque, A., N'Diaye, A. T. & Schmid, A. K. *Applied Physics Letters* **106**, 242404 (2015).

27 Boulle, O., Vogel, J., Yang, H., Pizzini, S., de Souza Chaves, D., Locatelli, A., Mentes, T. O., Sala, A., Buda-Prejbeanu, L. D., Klein, O., Belmeguenai, M., Roussigne, Y., Stashkevich, A., Cherif, S. M., Aballe, L., Foerster, M., Chshiev, M., Auffret, S., Miron, I. M. & Gaudin, G. *Nature Nanotechnology* **11**, 449-454 (2016).

28 Moreau-Luchaire, C., Mouta, S. C., Reyren, N., Sampaio, J., Vaz, C. A., Van Horne, N., Bouzehouane, K., Garcia, K., Deranlot, C., Warnicke, P., Wohlhuter, P., George, J. M., Weigand, M., Raabe, J., Cros, V. & Fert, A. *Nature Nanotechnology* **11**, 444-448 (2016).

29 Woo, S., Litzius, K., Kruger, B., Im, M. Y., Caretta, L., Richter, K., Mann, M., Krone, A., Reeve, R. M., Weigand, M., Agrawal, P., Lemesh, I., Mawass, M. A., Fischer, P., Kläui, M. & Beach, G. S. *Nature Materials* **15**, 501-506 (2016).

30 Kézsmárki, I., Bordács, S., Milde, P., Neuber, E., Eng, L. M., White, J. S., Rønnow, H. M., Dewhurst, C. D., Mochizuki, M., Yanai, K., Nakamura, H., Ehlers, D., Tsurkan, V. & Loidl, A. *Nature Materials* **14**, 1116 (2015).

31 Miron, I. M., Garello, K., Gaudin, G., Zermatten, P. J., Costache, M. V., Auffret, S., Bandiera, S., Rodmacq, B., Schuhl, A. & Gambardella, P. *Nature* **476**, 189-193 (2011).

32 Liu, L. Q., Pai, C. F., Li, Y., Tseng, H. W., Ralph, D. C. & Buhrman, R. A. *Science* **336**, 555-558 (2012).

33 Emori, S., Bauer, U., Ahn, S. M., Martinez, E. & Beach, G. S. *Nature Materials* **12**, 611-616 (2013).

34 Hoffmann, A. *IEEE Transactions on Magnetics* **49**, 5172-5193 (2013).

35 Hoffmann, A. & Bader, S. D. *Physical Review Applied* **4**, 047001 (2015).

36 Hellman, F., Axel Hoffmann, Yaroslav Tserkovnyak, Geoffrey Beach, Eric Fullerton, Chris Leighton, Allan MacDonald, Dan Ralph, Dario Arena, Hermann Dürr, Peter Fischer, Julie Grollier, Joseph Heremans, Tomas Jungwirth, Alexey Kimmel, Bert Koopmans, Ilya Krivorotov, Steven May, Amanda Petford-Long, James Rondinelli, Nitin Samarth, Ivan Schuller, Andrei Slavin, Mark Stiles, Oleg Tchernyshyov, Andre Thiaville & Zink, B. *Review of Modern Physics* **89**, 025006 (2017).

37 Jiang, W., Zhang, W., Yu, G. Q., Jungfleisch, M. B., Upadhyaya, P., Somaily, H., Pearson, J. E., Tserkovnyak, Y., Wang, K. L., Heinonen, O., te Velthuis, S. G. E. & Hoffmann, A. *AIP Advances* **6**, 055602 (2016).

38 Jiang, W., Xichao, Z., Guoqiang Yu, Wei Zhang, Xiao Wang, M. Benjamin Jungfleisch, John E. Pearson, Xuemei Cheng, Olle Heinonen, Kang L. Wang, Yan Zhou, Axel Hoffmann & te Velthuis, S. G. E. *Nature Physics* **13**, 162-169 (2017).

39 Yu, G., Upadhyaya, P., Shao, Q., Wu, H., Yin, G., Li, X., He, C., Jiang, W., Han, X., Amiri, P. K. & Wang, K. L. *Nano Letters* **17**, 261-268 (2017).

40 Yu, G. Q., Upadhyaya, P., Li, X., Li, W. Y., Kim, S. K., Fan, Y. B., Wong, K. L., Tserkovnyak, Y., Amiri, P. K. & Wang, K. L. *Nano Letters* **16**, 1981-1988 (2016).

41 Soumyanarayanan, A., M. Raju, A.L. Gonzalez Oyarce, Anthony K.C. Tan, Mi-Young Im, A.P. Petrovic, Pin Ho, K.H. Khoo, M. Tran, C.K. Gan, F. Ernult & Panagopoulos, C. *Nature Materials* **16**, 898 (2017).

42 Jaiswal, S., Litzius, K., Lemesh, I., Buttner, F., Finizio, S., Raabe, J., Weigand, M., Lee, K., Langer, J., Ocker, B., Jakob, G., Beach, G. S. D. & Klaui, M. *Applied Physics Letters* **111**, 022409 (2017).

43 Litzius, K., Ivan Lemesh, Benjamin Krüger, Pedram Bassirian, Lucas Caretta, Kornel Richter, Felix Büttner, Koji Sato, Oleg A. Tretiakov, Johannes Förster, Robert M. Reeve, Markus Weigand, Iuliia Bykova, Hermann Stoll, Gisela Schütz, Geoffrey S. D. Beach & Kläui, M. *Nature Physics* **13**, 170-175 (2017).

44 He, M., Peng, L. C., Zhu, Z. Z., Li, G., Cai, J. W., Li, J. Q., Wei, H. X., Gu, L., Wang, S. G., Zhao, T. Y., Shen, B. G. & Zhang, Y. *Applied Physics Letters* **111**, 202403 (2017).

45 Pai, C. F., Liu, L. Q., Li, Y., Tseng, H. W., Ralph, D. C. & Buhrman, R. A. *Applied Physics Letters* **101**, 122404 (2012).

46 Yu, J., Qiu, X., Wu, Y., Yoon, J., Deorani, P., Besbas, J. M., Manchon, A. & Yang, H. *Scientific Reports* **6**, 32629 (2016).

47 Yu, X. Z., Mostovoy, M., Tokunaga, Y., Zhang, W. Z., Kimoto, K., Matsui, Y., Kaneko, Y., Nagaosa, N. & Tokura, Y. *Proceedings of the National Academy of Sciences of the United States of America* **109**, 8856-8860 (2012).

48 Seki, S., Yu, X. Z., Ishiwata, S. & Tokura, Y. *Science* **336**, 198-201 (2012).

49 Rajeswari, J., Huang, P., Mancini, G. F., Murooka, Y., Latychevskaia, T., McGrouther, D., Cantoni, M., Baldini, E., White, J. S., Magrez, A., Giamarchi, T., Ronnow, H. M. & Carbone, F. *Proceedings of the National Academy of Sciences of the United States of America* **112**, 14212-14217 (2015).

50 Zhao, X., Jin, C., Wang, C., Du, H., Zang, J., Tian, M., Che, R. & Zhang, Y. *Proceedings of the National Academy of Sciences of the United States of America* **113**, 4918-4923 (2016).

51 Phatak, C., Heinonen, O., De Graef, M. & Petford-Long, A. *Nano Letters* **16**, 4141 (2016).

52 Zhang, S., Petford-Long, A. K. & Phatak, C. *Scientific Reports* **6**, 31248 (2016).

53 McVitie, S., Hughes, S., Fallon, K., McFadzean, S., McGrouther, D., Krajnak, M., Legrand, W., Maccariello, D., Collin, S., Garcia, K., Reyren, N., Cros, V., Fert, A., Zeissler, K. & Marrows, C. H. *Scientific Reports* **8**, 5703 (2018).

54 Nayak, A. K., Kumar, V., Ma, T. P., Werner, P., Pippel, E., Sahoo, R., Damay, F., Rossler, U. K., Felser, C. & Parkin, S. S. P. *Nature* **548**, 561 (2017).

55 Grundy, P. J. & Herd, S. R. *Physica Status Solidi A: Applied Research* **20**, 295 (1973).

56 Yu, X. Z., Tokunaga, Y., Kaneko, Y., Zhang, W. Z., Kimoto, K., Matsui, Y., Taguchi, Y. & Tokura, Y. *Nature Communications* **5**, 3198 (2014).

57 Yu, X. Z., DeGrave, J. P., Hara, Y., Hara, T., Jin, S. & Tokura, Y. *Nano Letters* **13**, 3755-3759 (2013).

58 Petford-Long, A. K. & De Graef, M. (John Wiley & Sons, Inc., 2012).

59 Beleggia, M., Schofield, M. A., Volkov, V. V. & Zhu, Y. *Ultramicroscopy* **102**, 37-49 (2004).

60 Graef, M. D. *Introduction to conventional transmission electron microscopy*. (Cambridge University Press, 2003).

61 Beleggia, M. & Zhu, Y. *Philosophical Magazine* **83**, 1045-1057 (2003).

62 Benitez, M. J., Hrabec, A., Mihai, A. P., Moore, T. A., Burnell, G., McGrouther, D., Marrows, C. H. & McVitie, S. *Nature Communications* **6**, 8957 (2015).

63 Shawn D. Pollard, Joseph A. Garlow, Jiawei Yu, Zhen Wang, Yimei Zhu & Yang, H. *Nature Communications* **8**, 14761 (2017).

64 Parratt, L. G. *Physical Review* **95**, 359-369 (1954).

65 Bjorck, M. & Andersson, G. *J Appl Crystallogr* **40**, 1174-1178 (2007).

66 Vansteenkiste, A., Leliaert, J., Dvornik, M., Helsen, M., Garcia-Sanchez, F. & Van Waeyenberge, B. *Aip Advances* **4**, 107133 (2014).

67 Legrand, W., Chauleau, J. Y., Maccariello, D., Reyren, N., Collin, S., Bouzehouane, K., Jaouen, N., Cros, V. & Fert, A. *Science Advances* **4**, 0415 (2018).

68 Heide, M., Bihlmayer, G. & Blügel, S. *Physical Review B* **78**, 140403(R) (2008).

69 Hrabec, A., Porter, N. A., Wells, A., Benitez, M. J., Burnell, G., McVitie, S., McGrouther, D., Moore, T. A. & Marrows, C. H. *Physical Review B* **90**, 0204402(R) (2014).

Figure captions

Table 1. Parameters characterizing the sample structure as determined from analysis of the X-ray reflectivity data. t_n is the nominal thickness, Δt denotes the roughness at the top interface of each layer, and t is the average thickness of each layer.

Layers		Parameters	
Capping Pt (t_n = 15 Å)		Δt	3.8 Å
		t	16.9 Å
8 x	W (t_n =10 Å)	Δt	4.8 Å
		t	10.1 Å
	Co (t_n =10 Å)	Δt	5.5 Å
		t	9.3 Å
	Pt (t_n =15 Å)	Δt	3.5 Å
		t	16.5 Å
Buffer Ta (t_n = 20 Å)		Δt	9.3 Å
		t	22.7 Å

Fig. 1. Simulation of Néel-type magnetic skyrmions with opposite chirality with spins pointing towards [A-(1)] or out from [B-(1)] the core direction. Blue color in regime R_3 represents magnetization of downwards normal to the plane (-1), grey color in regime R_1 represents magnetization upwards normal to the plane (+1). Red arrows in regime R_2 represents the spin configuration in the transition regime (also defined as the domain wall), which determines the topology of the spin textures. Theoretical calculated magnetic contrast of Néel-type skyrmions at a tilting angle of $\Phi = \pm 60^{\circ}$, no sample tilt ($\Phi = 0^{\circ}$). Magnetic contrasts are only visible when the sample is tilted, but the configurations seen in [A-(2)]/[B-(2)] and [A-(4)]/[B-(4)] appear indistinguishable. Adding them together enables the cancellation of the contribution from in-plane components and results in a slight contrast difference for different Néel-type skyrmions.

Figure 2. Structural and magnetic characterization of the magnetic multilayer. Inversion asymmetric magnetic multilayers with nominal thickness Ta(2 nm)/[Pt(1.5 nm)/Co(1 nm)/W(1 nm)]$_8$/Pt(1.5 nm) were deposited onto both SiN_x and SiO_2 substrates, shown in Fig. 2A. The high quality of films was confirmed by a X-ray reflectivity measurements (red dots), in which superlattice peaks up to the third order are observed, shown in Fig. 2B. The fitted reflectivity curve (blue line) obtained with the Parratt formalism using GenX software,[64,65] which enables the roughness (Δt), and the thickness (t) to be determined, summarized in Table 1. Inset to Fig. 2B is the corresponding hysteresis loop acquired with the applied magnetic field normal to the sample plane.

Figure 3. Experimental identification of room-temperature Néel-type skyrmions in the absence of magnetic field. Without tilting in the under-focus mode, no observable magnetic contrast is present – consistent with the theoretical expectation of Néel-type skyrmions, as shown in Fig. 3B. By tilting the sample of $\Phi = -30^{\circ}$ shown in Fig. 3A, the presence of (stripes/skyrmions) Néel-type spin textures were revealed. The magnetic contrast of these spin textures - the upper left corner (black)/lower right corner (white) is reversed upon the inversion of tilting angle to $\Phi = +30^{\circ}$, as shown in Fig. 3C. Slices along the diagonal direction of the selected skyrmion further illustrates this, as shown in Fig. 3D. The distance between two dashed lines corresponds to the diameter of skyrmions.

Figure 4. Evolution of the Néel-type skyrmions sizes as a function of perpendicular magnetic fields. The magnetic field dependent Lorentz TEM imaging results are shown in Figs. 4A–D, from which one notices that the increasing of perpendicular magnetic fields results in the shrinking/annihilation of skyrmions. The change of diameter of selected skyrmions as a function of field (marked by green arrows in Fig. 4A) is further shown in Fig. 4E.

Figure 5. The reduced single skyrmion energy $\widehat{U}$ calculated for different values of the DMI strength D_k (black short dashed/dotted curves) based on the effective medium model at applied magnetic fields (A) 25 mT, (B) 21 mT, (C) 12.1 mT, and (D) 7.6 mT. The sizes of the individual skyrmions from Fig. 6E that were labeled as S_{k1} - S_{k5}, are shown at each field as vertical colored long dashed lines. A DMI value D_k = 1.5 ± 0.2 mJ/m^2 (black thick dotted curves) is inferred, as at this value the experimental skyrmion sizes lie within the minimum energy valley for all applied field.

Figure 6. Micromagnetic simulation results of the skyrmion sizes as a function of perpendicular magnetic fields. The dashed line located at 74 nm represents the minimum diameter. Insets show the m_z profile of a skyrmion with D_k = 1.6 mJ/m^2. The left inset corresponds to the spin profile of a skyrmion with a large inner core at 6 mT, and the right inset represents the spin profile of a compact skyrmion at 45 mT, respectively.

Figure 1

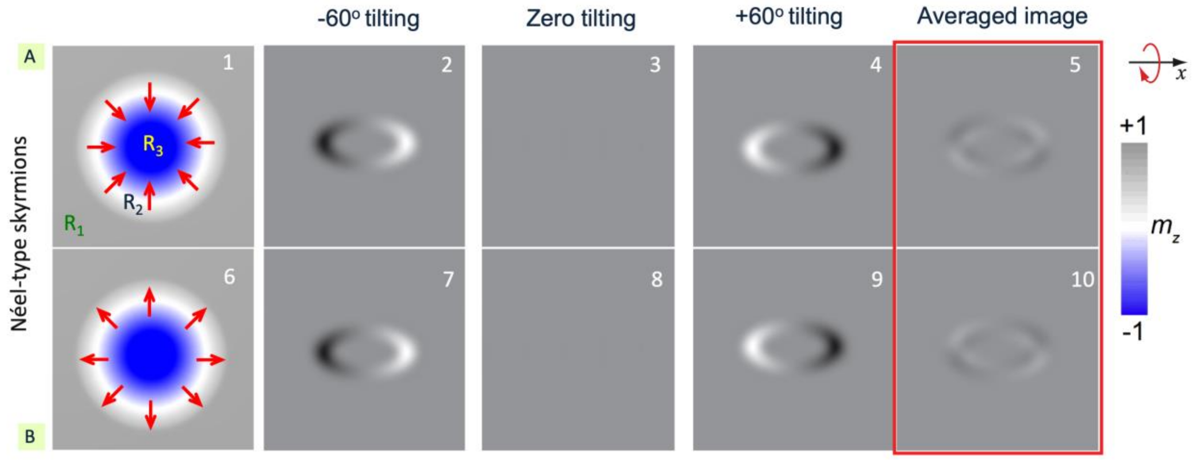

Figure 2

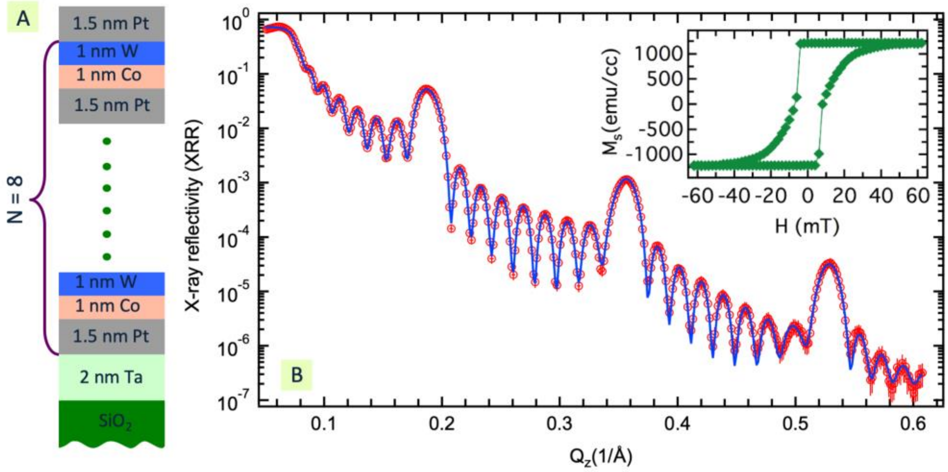

Figure 3

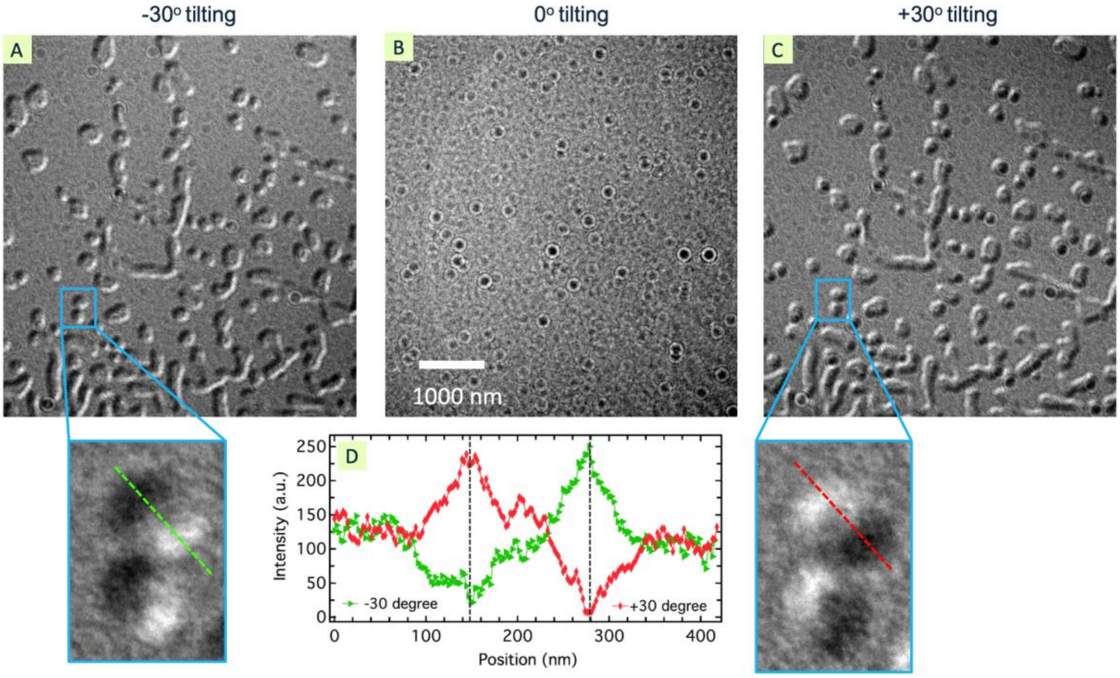

Figure 4

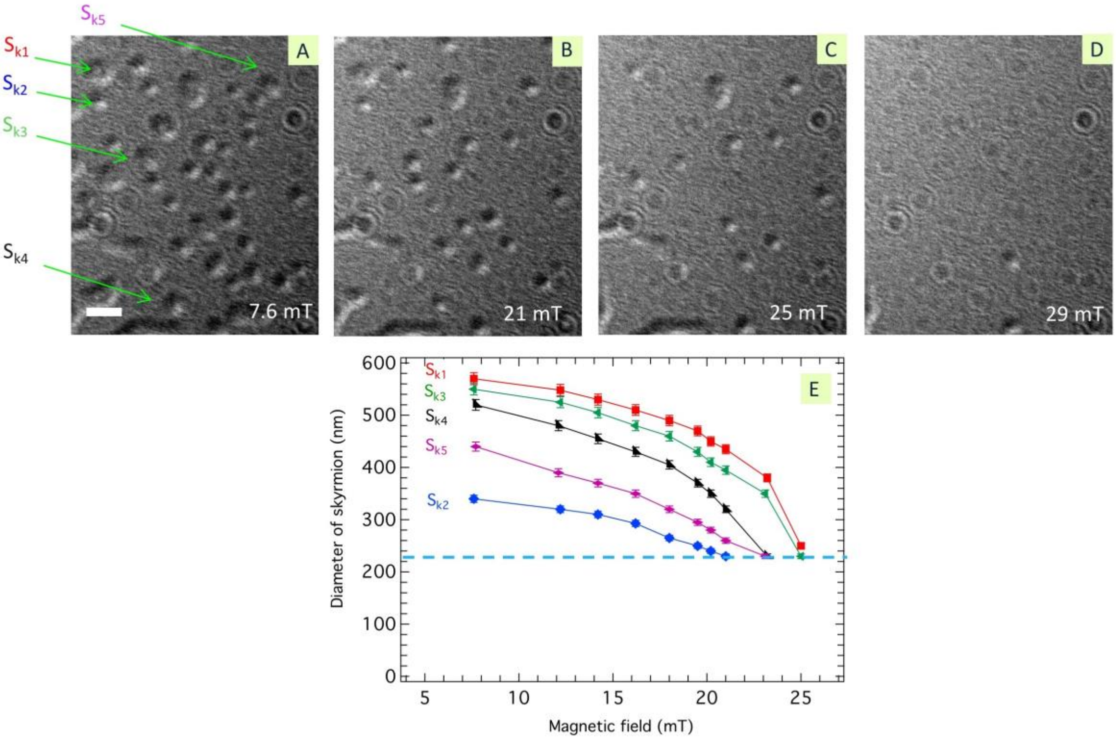

Figure 5

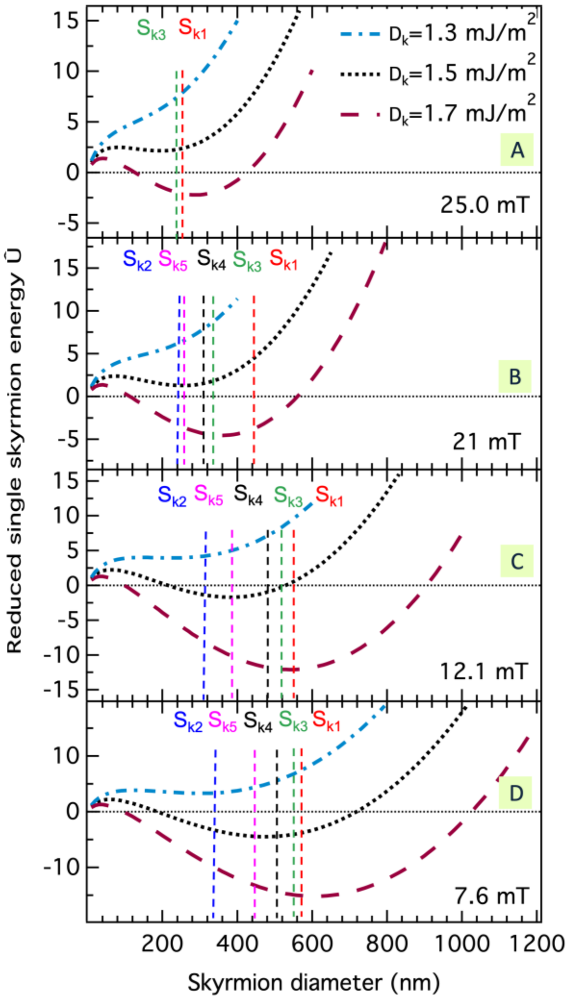

Figure 6